Diamond & Related Materials 17 (2008) 1021–1028

Contents lists available at ScienceDirect

Diamond & Related Materials

journal homepage: www.elsevier.com/locate/diamond

New insights into the mechanism of CVD diamond growth: Single crystal diamond in MW PECVD reactors

Yu. A. Mankelevich [a], P.W. May [b,*]

[a] Nuclear Physics Institute, Moscow State University, 119991 Moscow, Russia
[b] School of Chemistry, University of Bristol, Bristol BS8 1TS, United Kingdom

ARTICLE INFO

Available online 3 April 2008

Keywords
CVD diamond
MW discharge
Modeling
Single crystal growth

ABSTRACT

CVD Diamond can now be deposited either in the form of single crystal homoepitaxial layers, or as polycrystalline films with crystal sizes ranging from mm, µm or nm, and with a variety of growth rates up to 100s of µm h^{-1} depending upon deposition conditions. We previously developed a model which provides a coherent and unified picture that accounts for the observed growth rate, morphology, and crystal sizes, of *all* of these types of diamond. The model is based on competition between H atoms, CH_3 radicals and other C_1 radical species reacting with dangling bonds on the diamond surface. The approach leads to formulae for the diamond growth rate *G* and average crystallite size $<d>$ that use as parameters the concentrations of H and CH_x $(0 \le x \le 3)$ near the growing diamond surface. We now extend the model to show that the basic approach can help explain the growth conditions required for single crystal diamond films at pressures of 100–200 Torr and high power densities.

© 2008 Elsevier B.V. All rights reserved.

1. Introduction

Diamond films can be deposited using a chemical vapour deposition (CVD) process involving the gas-phase decomposition of a gas mixture containing a small quantity of a hydrocarbon in excess hydrogen [1]. A typical gas mixture uses 1% CH_4 in H_2, and this produces polycrystalline films with grain sizes in the micron or tens of micron range, depending upon growth conditions, substrate properties and growth time. It is generally believed [2,3] that the main growth species in standard diamond CVD is the CH_3 radical, which adds to the diamond surface following hydrogen abstraction by H atoms. Thus, a high concentration of atomic H at the surface in addition to CH_3 radicals is a prerequisite for successful microcrystalline diamond (MCD) deposition. By increasing the ratio of methane in hot filament (HF) CVD reactors from the standard 1% CH_4/H_2 gas mixture to ~5% CH_4/H_2, the grain size of the films decreases, and eventually becomes of the order of hundreds down to tens of nm. Such nanocrystalline diamond (NCD) films (often termed 'cauliflower' or 'ballas' diamond) are smoother than the microcrystalline ones, but have larger numbers of grain boundaries that contain substantial graphitic impurities. With further addition of CH_4, the films become graphitic.

Recently, so-called ultrananocrystalline diamond (UNCD) films have become a topic of great interest, since they offer the possibility of making smooth, hard coatings at relatively low deposition temperatures, which can be patterned to nm resolution [4,5]. These differ from NCD films [6] since they have much smaller grain sizes (~2–5 nm). Most reports of the deposition of these films describe using a microwave (MW) plasma CVD reactor and gas mixture of 1% CH_4 in Ar, usually with addition of 1–5% H_2 [4]. We have previously reported the use of similar $Ar/CH_4/H_2$ gas mixtures to deposit NCD (or UNCD) in a hot filament (HF) reactor [7], with the compositional diagram for mixtures of Ar, CH_4 and H_2 being mapped out corresponding to the type of film grown.

Originally it was suggested [8] that the C_2 radical played an important role in the growth mechanism for UNCD. However, recent work by ourselves [9,10] and others [11] has shown that C_2 is not a dominant species. In our previous paper [10], we used a 2-dimensional model of the gas chemistry, including heat and mass transfer, in our HF reactors to understand the experimental observations. The conclusions led to a generalised mechanism for the growth of diamond by CVD which was consistent with many experimental observations, both from our group and from others in the literature [12].

The proposed mechanism involves competitive growth by all the C_1 radical species that are present in the gas mixture close to the growing (100) diamond surface. Previous models mainly considered CH_3 since this is the dominant reactive hydrocarbon radical in standard H_2-rich CVD gas mixtures. However, we found that in HFCVD reactors at high filament temperatures (*e.g.* T_{fil}~2700 K) or high CH_4 concentrations, the concentration of the other C_1 radical species, in particular C atoms, near the growing diamond surface can become as high as ~10^{12} cm^{-3}, and so may contribute to the growth

* Corresponding author.
E-mail addresses: paul.may@bris.ac.uk (P.W. May), ymankelevich@mics.msu.su (Yu. A. Mankelevich).

0925-9635/$ – see front matter © 2008 Elsevier B.V. All rights reserved.
doi:10.1016/j.diamond.2008.03.022

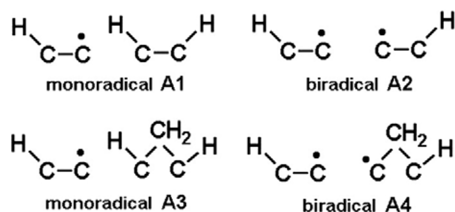

Fig. 1. The main types of radical site important for growth on a (100) diamond surface during CVD. The sites are labelled A1, A2, A3, and A4 following the scheme of Skokov *et al.* [18].

process. C atoms as gas-phase precursors of diamond films have been considered before for HFCVD [13], microwave CVD [14] and plasma arc jet reactors [13,15–17].

In most growth models, abstraction of surface H atoms by gas-phase atomic H are the reactions which drive the chemistry of growth. These reactions create two main types of surface radical sites on the reconstructed (100)−(2×1) diamond surface [18] (see Fig. 1), monoradical sites (a single dangling bond on a surface carbon) and biradical sites (defined as two surface radical sites on adjacent carbons). There are different variants of these bi- and monoradical sites, depending upon the local surface geometry, and the most important for growth have been labelled as A1, A2, *etc.*, in Fig. 1. For typical diamond CVD conditions, the fraction of available biradical sites (of all types) is ~10 times lower than that of the monoradical sites (see section 1.4, below).

1.1. Growth from CH_3

According to quantum-mechanical calculations [18] for a diamond (100) surface, CH_3 can add to dimer sites (both mono and biradical) but CH_3 cannot add to bridge and dihydride surface sites because of the strong steric repulsion among H atoms of the CH_3 group and the surrounding surface H atoms. In our previous studies [9,10,12] we have considered only addition of CH_3 to *biradical* dimer sites as the primary process by which carbon is added to the diamond lattice. Since the biradical sites have an adjacent dangling bond already present, the CH_3 adduct does not have to wait for a suitable abstraction reaction to occur before it can link in to the lattice. Thus, the reaction that forms the bridging CH_2 group readily occurs before the CH_3 can desorb. In ref. [12,17,19] we derived an equation for the growth rate contribution, G (in μm h^{-1}) from CH_3 via this biradical channel as:

$$G_{bi} = 3.8 \times 10^{-14} T_s^{0.5} [CH_3] R^2 \quad (1)$$

where T_s is the substrate temperature in K, $[CH_3]$ is the methyl gas-phase concentration in cm^{-3} at the substrate surface, and R is the fraction of surface monoradical sites (see section 1.4).

A modification to this previous model is that we now consider that, in addition to the biradical channel, CH_3 can also attach to monoradical dimer sites [18,20], thereby terminating the 'dangling bond' and forming a pendant CH_3 adduct. There are then two competing processes which determine the fate of this adduct. One is that the adduct can simply desorb back into the gas phase (which is likely to be quite a facile process) and reform the monoradical site, and this can be quantified by a desorption rate, k_d. Alternatively, a suitable H abstraction reaction might occur on a neighbouring lattice position (or on an H atom from the CH_3 adduct) during the time the CH_3 remained attached to the surface followed by fast H atom transfer from the pendant CH_3 to this vacant site [18]. This suitable H abstraction reaction would depend upon the gas-phase atomic hydrogen concentration above the surface, [H], and the rate would be given by k_a[H], where k_a is the rate constant for abstraction. Then, the pendant CH_2 will create a dangling bond to the adjacent carbon of the same dimer (as a result of a β-scission reaction) and thus, the pendant CH_2 will be incorporated into the lattice as a bridging CH_2 group [18]. Thus, for successful incorporation of CH_3 into the diamond lattice via monoradical sites, the rate of H abstraction must be comparable with or higher than the CH_3 desorption rate, *i.e.* $k_a[H] \geq k_d$. We have now included this mechanism by adding two monoradical channels to Eq. (1). The channels involve two main monoradical sites during regular growth, a dimer–dimer pair (A1 in Fig. 1) and a dimer–bridge pair (A3 in Fig. 1). We also assume that time-averaged fraction of these sites are 50%, and the rate of the CH_3 absorption on these monoradical dimer sites is the same as for biradical sites [12] (8.3×10^{-12} cm^{-3} s^{-1} for T_s = 1200 K). To derive an expression for the growth rate, G_{mono}, via monoradical dimer channels similar to that in Eq. (1), we should change R^2 (the probability of the surface site becoming a biradical site) in Eq. (1) to R (the probability of the monoradical surface site), and multiply by the probability of CH_3 incorporation via monoradical channels, given by $k_a[H]/(k_a[H]+k_d)$. Thus, we will have

$$G_{mono} = 3.8 \times 10^{-14} T_s^{0.5} [CH_3] \times R \times 0.5 \cdot k_a[H]\{1/(k_a[H] + k_d(A1)) + 1/(k_a[H] + k_d(A3))\} \quad (2)$$

and the total growth rate due to CH_3 can now be expressed as

$$G_{CH3} = 3.8 \times 10^{-14} T_s^{0.5} [CH_3] \cdot R \cdot \{0.5 \cdot k_a[H] \cdot (1/(k_a[H] + k_d(A1)) + 1/(k_a[H] + k_d(A3))\ ) + R\} \quad (3)$$

where k_d(A1) and k_d(A3) refer to the rates of desorption of CH_3 from A1 and A3 sites, respectively. R is the fraction of surface monoradical sites given by $R = C_d^*/(C_d^* + C_dH)$, where C_d^* and C_dH are the respective densities of open- and hydrogen-terminated surface sites. This fraction, R, mainly depends on the rate constants for the surface H abstraction and addition reactions. Neglecting the effects of CH_x upon radical site density R, we obtain [9]

$$R = 1/\{1 + 0.3 \exp(3430/T_s) + 0.1 \exp(-4420/T_s)[H_2]/[H]\} \quad (4)$$

where [H] and $[H_2]$ are the atomic and molecular hydrogen gas-phase concentrations at the substrate surface, respectively.

We can now estimate the relative importance of the monoradical and biradical growth processes for CH_3 for different diamond CVD conditions. Using the values of k_a from ref. [12], and k_d(A1) and k_d(A3) from ref. [18] for a typical substrate temperature of T_s = 1200 K, we see that the CH_3 incorporation rate via the monoradical dimer sites A1 and A3 will be equal to the biradical incorporation rate when $[H] = 2Rk_d(A1)/((1-R) \cdot k_a)$ and when $[H] = 2Rk_d(A3)/((1-R) \cdot k_a)$, respectively. For R ~ 0.1 (see later) this condition will occur when $[H] = 1.8 \times 10^{14}$ cm^{-3} for the A1 site ($k_d = 5300$ s^{-1} [18]) and when $[H] = 5.2 \times 10^{15}$ cm^{-3} for the A3 site ($k_d = 1.5 \times 10^5$ s^{-1} [18]).

Our simulations show that [H] ~ 10^{14}–10^{15} cm^{-3} for typical MCD growth conditions in HFCVD and MW PECVD reactors, therefore CH_3 incorporation via biradical and monoradical sites could be comparable for this case. In contrast, for SCD growth in high power MWCVD reactors [H] ~ 10^{16} cm^{-3}, and thus, CH_3 incorporation via monoradical sites will now be the dominant mechanism. However, we note that accurate estimation of the contributions from both channels (mono and biradical) requires reliable values of [H] (and k_d for the monoradical channel) and its substrate temperature dependences.

1.2. Growth from CH_x

As well as CH_3 addition, we assume that CH_x (x<3) species, (C atoms, CH radicals, and also CH_2 although its number density close to the substrate surface is much lower) could also adsorb onto the surface. CH_x species can readily attach to *both* surface biradical sites and monoradical sites. These CH_x radicals differ from CH_3 in that after bonding to the surface they still have at least one 'spare' dangling bond and thus remain highly reactive. In the case of monoradical sites, once

attached, the reactive adduct does not have to wait for a subsequent H abstraction reaction — it simply utilizes its spare dangling bond to react with an adjacent carbon and link into the lattice. This will also occur on biradical sites in much the same way. Therefore, CH_x species can be readily incorporated into the diamond lattice via both monoradical and biradical sites. The result of this is that even for low CH_x concentrations $[CH_x]/[CH_3]\sim R+k_a[H]/(k_a[H]+k_d)$, their contribution to the growth rate can become important since they can readily add to the more abundant radical sites.

In a similar manner to Eqs. (2) and (3), it is possible to estimate the contribution to the growth rate, G (in μm h^{-1}), of these CH_x species, using formulae stated in refs. [12,17,19]:

$$G_{CHx} = 3.9\times10^{-14}T_s^{0.5}[CH_x]R \tag{5}$$

where CH_x is for x=0,1,2.

1.3. The fate of CH_2 bridging groups

We now consider the fate of the bridging CH_2 groups. From the stable bridging structures, further hydrogen abstraction reactions allow the CH_2 groups to migrate across the surface until they meet a step-edge, at which point they will extend the diamond lattice, leading to large regular crystals [10,12,18]. In contrast, many of the bridging structures created following addition of C and CH species would remain reactive since they still contain at least one dangling bond. The most likely fate for such reactive surface sites, considering that they are surrounded by a gas mixture containing a high concentration of H atoms, is that they are rapidly hydrogenated to CH_2. If so, the subsequent reactions will be indistinguishable from attachment and growth by methyl, as described above. The rate of these hydrogenation reactions can be estimated by reference to an analogous gas-phase reaction, such as: $C_2H_4+H+M\rightarrow C_2H_5\ C_2H_5+M$. The high-pressure limit of this reaction rate is $k^*[M]\sim5\times10^{-12}$ cm^{3}s^{-1} at $T\sim1000$ K [21]. The characteristic time of this reaction (given by $\tau\sim(k[M][H])^{-1}$) for typical MCD growth conditions ($[H]\sim2\times10^{14}$ cm^{-3}, $[CH_3]\sim10^{13}$ cm^{-3}, T_s=1200 K and $R\sim0.1$) is $\tau\sim1$ ms, which is comparable with the characteristic time for H abstraction $\tau\sim(k_a[H])^{-1}\sim0.8$ ms and much lower than that for CH_3 adsorption $\tau\sim(k_{ad}[CH_3]R)^{-1}\sim120$ ms.

However, when the atomic H concentration is low, other possible fates for the reactive surface adducts are possible, such as reaction with other gas-phase hydrocarbon radicals, further bridging or cross-linking leading to restructuring of the surface, or even renucleation of a new, misoriented crystallite. These processes are proposed to be one route by which the size of crystallites is prevented from becoming larger.

For the typical conditions used to deposit MCD/NCD and UNCD in a variety of different diamond CVD reactors (including MW and HF CVD reactors), the reactions of the surface adducts with atomic hydrogen which lead to continuous normal diamond growth are much more frequent events than the surface reactions which might ultimately lead to renucleation. As long as the surface migration of CH_2 (induced by H abstractions) is much faster than adsorption of CH_3, the aggregation of CH_2 bridge sites into continuous chains (void filling) will provide normal layer-by-layer {100} diamond growth [18]. But as the ratio of gaseous CH_x/H increases, the initiation of next layer growth could proceed before all the voids in the current layer are filled. Thus, depending upon the gas mixture and reaction conditions used, the relative concentrations of each of these species close to the growing diamond surface (*e.g.* $[H]/[CH_3]$, $[H]/[C]$, $[H]/[H_2]$) determine the probability of a renucleation event occurring and the average equilibrium crystal sizes, $\langle d\rangle$, and hence the morphology of the subsequent film.

1.4. Surface radical sites

We extended these ideas [12] to derive quantitative estimations of $\langle d\rangle$. Fig. 2 shows the percentage of both types of open sites for

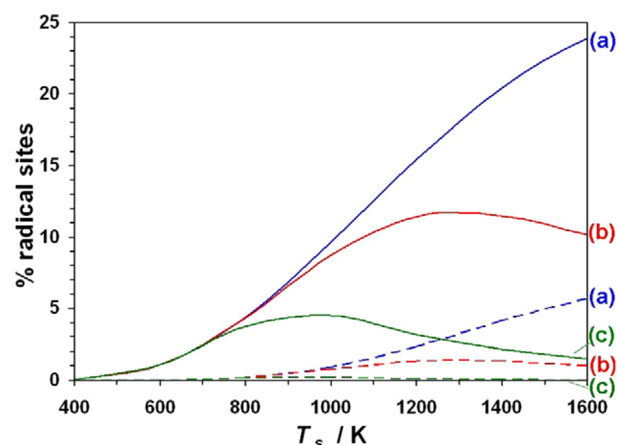

Fig. 2. Values of the percentage of monoradical sites R (full lines), and biradical sites R^2 (dashed lines) on a diamond surface calculated using Eq. (3), using values of $[H_2]/[H]$ of (a) 10, (b) 100 and (c) 1000. The values of $[H_2]_s/[H]_s$ are ~180 for the extremely hot plasma conditions and ~680 for the hot plasma condition, described in section 2 which falls between curves (b) and (c), giving R~9% and R^2~1%.

different substrate temperatures and $[H_2]/[H]$ ratios, and helps to explain the diamond growth behaviour observed at different temperatures. At standard CVD growth temperatures of ~1200 K, and values of $[H_2]/[H]$=1000 (typical of CVD diamond growth [9]), ~12% of the diamond surface is covered with monoradical sites, but only ~1.5% of the surface has the biradical sites necessary for CH_3 addition via the biradical channel (Fig. 2(b)).

The relative contributions for incorporation of CH_3 via monoradical and biradical channels depend mainly on the substrate temperature and on [H]. As can be seen from Eqs. (1) and (2), the following trends should be observed: high [H] will promote the monoradical channel, whereas higher desorption rates k_d will reduce the monoradical channel contribution.

The percentages for R and R^2 shown in Fig. 2(b) highlight why diamond CVD is often a slow process under conditions where CH_3 is the only possible growth species. These percentages are a sensitive function of temperature, however, and for lower temperatures, the number of radical sites (of both types) falls rapidly. The MCD growth rate, G, has an activation energy $E\sim20$–30 kcal mol^{-1} [22] ($G\sim\exp(-E/(0.001987\,T_s))$) at $T_s<1200$ K and drops an order of magnitude for each ~200 K decrease in T_s (*e.g.* for $T_s\sim1000$ K, ~800 K). The percentage of biradical sites drops accordingly with decreasing T_s and, in addition, CH_3 concentrations are reduced at low temperatures because of three-body recombination of CH_3 with H atoms. Note, however, that UNCD and NCD can be deposited (slowly) in MW PECVD reactors in 1% CH_4/Ar mixtures at temperatures down to ~700 K [5]. Here the other C_1 species (C atoms) could be the main contributors to growth [10], because these only require monoradical sites with corresponding activation energy $E\sim6.9$ kcal mol^{-1} ($G\sim R\sim\exp(-E/(0.001987\,T_s))$, Eqs. (4)–(5). R has a small but non-zero value ($R\sim3\%$), even at these low temperatures: for higher $[H_2]/[H]$ ratios (*e.g.* Fig. 2(c)), the value of R^2 at all temperatures is too low for growth by CH_3 alone, but R is sufficient that growth from the other C_1 species is still possible, even down to temperatures as low as $T_s\sim700$ K. This is consistent with the fact that literature reports of low temperature growth often describe that the films consist of low quality, defective, small grains, with high sp^2 carbon content, and/or NCD-type material [23,24]. It should be noted that experimentally observed values of E are in the range $E\sim2$–8 kcal mol^{-1} [5].

Conversely, for the very low $[H_2]/[H]$ values ~100 that might occur in high power plasmas, R and R^2 values (Fig. 2(a)) can both become too high, resulting in localised cross-linking and restructuring of the diamond surface, which ultimately lead to graphitisation and/or amorphisation of the surface. This can largely be prevented, however, by growing at lower substrate temperatures <1000 K, where the R and

R^2 values are sufficient to create the appropriate number of open sites (R ~ 10%, R^2 ~ 1%), but not enough to initiate amorphisation.

1.5. Crystal size estimation

Turning now to the question of crystallite size, by comparing the frequency of CH_2 surface migration processes with those for CH_x addition, we can estimate the average crystal size corresponding to varying deposition conditions. Assuming that the ratio of $[H]/[H_2]$ near the substrate is not extremely low (*e.g.* $[H]/[H_2]>0.001$, as will be the case for the vast majority of CVD deposition reactors), the average crystal size in nm, is given by [12]:

$$\langle d \rangle = \{2+0.6\,\exp(3430/T_s)\}\times\{[H]/\textstyle\sum CH_x\} \quad (x<4) \tag{6}$$

This equation predicts that the average crystal size is a linear function of the ratio of the concentration of atomic H to those of the C_1 growth species, close to the growing surface. Previously, [12] we used Eqs. (1), (5) and (6) to model the growth rate, G, and maximum crystal size $\langle d \rangle$ for films grown under various conditions in hot filament CVD reactors. We showed that the predictions of these equations for both G and $\langle d \rangle$ compared favourably with the experimental values under both MCD and NCD growth conditions. However, when the nucleation rate approached that required for UNCD growth, the model became less accurate — although it still predicted grain sizes to within an order of magnitude, as well as the trends in growth rate and grain size with distance from the filament.

One process which has not been included in the model so far, and which would affect the rate of defect formation on the surface, is that of surface reconstruction or cross-linking. This was mentioned earlier as one possible fate for reactive surface adducts when there are insufficient H atoms nearby to rapidly hydrogenate any dangling bonds to form stable CH_2 bridges. Thus, the likelihood of a surface defect being created – possibly leading to formation of a new crystallite with different symmetry to the underlying lattice – will be directly related to the concentration (or adsorption reaction probability) of CH_x ($x<4$) and/or more complex hydrocarbon radicals C_yH_z ($y>1$), but inversely related to the concentration of H close to the surface. Thus, Eq. (6) can be multiplied by an additional factor to give:

$$\langle d \rangle_{new} = \{2+0.6\,\exp(3430/T_s)\}\times\{[H]/\textstyle\sum[CH_x]\} \times [H]/\{f_1([CH_x])+f_2([C_yH_z])\} \tag{7}$$

for $x<4$, $y>1$ and where f_1 and f_2 are 'efficiency functions' which determine how efficient these defect creation processes are. As a first approximation, since these functions are unknown and might be a function of deposition conditions, in this paper we shall consider only the effect of CH_x ($f_2=0$) and shall assume that $f_1([CH_x])=\Sigma[CH_x]$.

We should make it clear that the value of $\langle d \rangle_{new}$ calculated here would be the *equilibrium*, *ultimate* or *limiting* value that would be achieved after the growth had occurred for sufficient length of time that any effects due to the substrate material, surface topology, and nucleation methods can be neglected. For SCD this is not an issue since columnar growth does not occur and crystallite size is independent of growth time. It is also not an issue with cauliflower NCD or UNCD, where renucleation occurs continually and there is no increase in crystallite size with growth time. However, when columnar growth occurs, such as during MCD deposition, the crystal size increases with growth time. Thus, in comparing our predictions with experimental data for MCD, we must be careful to ensure that the growth time was sufficiently long that that an equilibrium between the rate of secondary nucleation and the rate of crystal size increase had been reached.

Fig. 3 shows the predictions of Eq. (7) as a function of $[H]/[\Sigma CH_x]$, plotted on a log-scale to allow all the diamond growth regions to be displayed on the same graph. The figure demonstrates that the type of film (SCD, MCD, NCD or UNCD) is determined simply by the $[H]/[\Sigma CH_x]$ ratio near the growing diamond surface. Low $[H]/[\Sigma CH_x]$ ratios and elevated substrate temperatures will favour smaller crystal sizes, and thereby promote NCD and UNCD deposition. However, should the atomic H concentration fall too low, then diamond growth ceases ($\langle d \rangle \rightarrow 0$), as observed in our and other experiments [7]. For $[H]/[\Sigma CH_x]$ values less than ~1, $\langle d \rangle$ becomes <10 nm, which is consistent with UNCD. For $[H]/[\Sigma CH_x]$ between 1 and 3, $\langle d \rangle$ is between 10 and 100 nm, which is NCD. For $[H]/[\Sigma CH_x]$ values higher than 3, the crystal size approaches a few μm, so this is the MCD regime. And, extrapolating the graph, for $[H]/[\Sigma CH_x]$>~60 the crystallite size becomes >100 μm, which is approaching SCD. It should be noted that some other mechanism of crystal size limitation could occur for UNCD deposition in MW PECVD reactors in methane–hydrogen mixtures in excess (up to 99%) Ar (*e.g.* renucleation due to C_2 [5] and thus $f_2 \neq 0$ in Eq. (7) for this case). Preliminary simulations of UNCD growth in 0.5% CH_4/1% H_2/Ar mixtures of our MW PECVD reactor show that C atoms are the dominant species above the substrate. The calculated concentrations $[C]\sim10^{12}$ cm^{-3} and $[H]\sim10^{15}$ cm^{-3} provide growth rates $G\sim0.1$ μm h^{-1}, which are close to those experimentally observed.

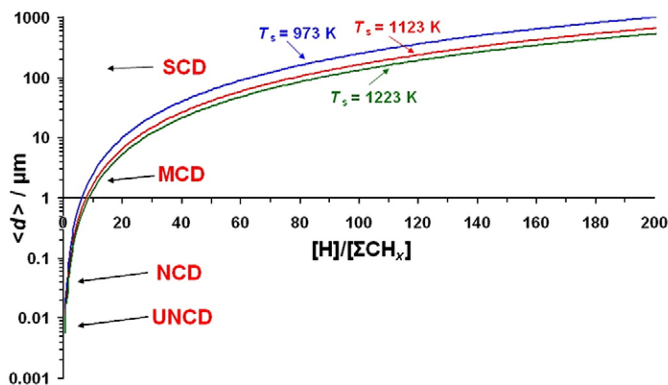

Fig. 3. A log-plot of average diamond crystal size $\langle d \rangle_{new}$ calculated using Eq. (7) against the ratio of the concentrations of atomic hydrogen to all the other C_1 hydrocarbon radicals ΣCH_x ($x<4$) close to the growing diamond surface, for three substrate temperatures, T_s. For the purposes of this figure, UNCD has been arbitrarily defined as diamond with crystal size <10 nm, NCD as <100 nm, and MCD>100 nm, with SCD being an extrapolation of the lines to $\langle d \rangle_{new}$ values of the order of 100's of μm or mm.

In this paper we shall concentrate on the SCD regime, and a full report of the results of the model for all other types of diamond film will be given elsewhere. From Fig. 3 we would predict that in order to achieve the $\langle d \rangle$ values of the order of many μm or even mm that are necessary for SCD growth, we require a very large ratio of $[H]/[\Sigma CH_x]$. However, in order to get a reasonable growth rate, $[CH_3]$ also needs to be large, which can be achieved using a high proportion of CH_4 in the gas mixture (2–10%) and higher pressures than the 20 Torr that are typical for HFCVD, such as 100–200 Torr. But in order to obtain the required $[H]/[CH_3]$ ratio at these higher pressures and methane concentrations, extremely high MW power densities (~40–150 W cm^{-3}) [25] would be required to create a high density plasma. The high gas temperatures (~3000–3400 K) this would produce should greatly increase the dissociation rate of H_2, leading to a larger concentration of atomic H at the growing surface (compared with that in the lower power plasmas used for depositing MCD). This high [H] ensures that any C_1 species that attach to the surface will be rapidly hydrogenated to CH_2 *before* they have chance to restructure the surface. This allows rapid growth (since *every* adsorbed C_1 species contributes to growth), together with essentially no renucleation, which leads to large crystal sizes. Thus, single crystal diamond should be grown – even at these high CH_4 concentrations – so long as the power density is high enough to maintain a very high [H] that is uniformly distributed above the substrate, and the (100) substrate itself is defect-free and cooled efficiently and uniformly to prevent overheating [26].

These predictions are all borne out by the experimental conditions reported by the few groups who have successfully grown SCD to date. For example, 270 μm-thick single crystal diamond films of area of 2.5×2.5 mm have been grown by the group at Hasselt University, at 700 °C using 10% CH_4 [27]. The same group has reported epitaxial diamond growth yielding sub-nm smooth surfaces for films with thicknesses up to 730 μm [28]. Using similar conditions, freestanding diamond films of area 4×4 mm^2 and thickness between 390 and 690 μm were reported by workers from Element Six [29]. Recently, a group based at the Carnegie Institute in Washington has grown single crystal diamond up to 4.5 mm in thickness at growth rates as much as two orders of magnitude higher than conventional polycrystalline CVD methods [30,31]. These single crystals can be fashioned into brilliant cut 'gemstones' using standard techniques. There are already companies (*e.g.* Apollo Diamond [32]) beginning to exploit the deposition conditions to produce CVD diamonds for the commercial gemstone market.

In this paper we seek to test our model using the key reactor parameters and conditions used for SCD growth on (100) substrates reported by Bogdan *et al.* [28]. They used a MW plasma reactor at a gas pressure of 180 Torr and methane concentration of 10% in H_2 with a total gas flow of 360 sccm, a substrate temperature of 973 K, input power of 600 W (giving an energy loading of 25 eV/molecule). They reported growth rates ~3–4 μm h^{-1}, and although the film surfaces were generally smooth with a very low quantity of defects, some round-shaped growth structures with heights up to 0.5 μm and widths up to 100 μm occurred in some parts of the smooth samples, sometimes with a small number (<2 mm^{-2}) of square-shaped inverted pits with fourfold symmetry of size <50 μm. Thus, their growth conditions are near SCD, but are not quite perfect.

2. 2D model and calculated results

In order to obtain the gas composition and the H and CH_x concentrations close to the surface that are required as inputs to Eqs. (1)–(7), we have developed a 2D model of a MW PECVD reactor to study SCD deposition processes and the effects of reactor parameters variations. We assume cylindrical symmetry, so the two important coordinates are *r*, the radial distance from the centre-line of the chamber, and *z*, the axial (vertical) height above the substrate surface. The model comprises three blocks, which describe (i) activation of the reactive mixture (*i.e.* electromagnetic fields and plasma parameters, power absorption and gas heating), (ii) gas-phase processes (heat and mass transfer, species diffusion and thermal diffusion and plasma-chemical kinetics), and (iii) gas-surface processes at the substrate. The set of non-stationary conservation equations for mass, momentum, energy and species concentrations was then solved numerically in (*r*,*z*) coordinates. Electromagnetic fields (*E*,*H*) are not calculated in this approach. Instead, a uniform or weakly non-uniform (~10%) distribution of electron temperature T_e is applied to a hemispherical or cylindrical volume, approximately corresponding to the observed (glowing) experimental plasma region. Because of the sharp exponential dependence of ionization rates and electronic densities from the reduced electric field *E*/*N* (where *N* is the gas concentration), a very narrow range of reduced electric fields *E*/*N* will be realised in a MW discharge plasma with given input power density levels. We determined the range of *E*/*N* for different gas temperatures between 2000 and 3300 K using a 0D model for the electron and plasma kinetics. In the 0D model, the balance equations for charged and neutral species are solved for different reduced electric fields. Simultaneously, the electron energy distribution function for the chosen gas mixture composition is calculated by solving the Boltzmann equation in a two-term approximation, using a set of known electron-particle collision cross-sections. As a result, the steady state species number densities, and rate coefficients of electron reactions as a function of T_e (or *E*/*N*) are obtained and used in the 2D model. Using different values of T_e we can simulate the conditions for different power densities and various total input powers for a given plasma volume. In the present 2D calculations, we have used a local equilibrium approach and calculated the absorbed power density directly as a sum of power losses and gains in various electron-particle reactions (such as electronic, vibrational and rotational excitation/de-excitation, dissociation, ionization):

$$Q_J = \sum_i k_i N_j n_e \varepsilon_i \qquad (9)$$

Here, ε_i is the electron energy loss ($\varepsilon_i>0$) or gain ($\varepsilon_i<0$) in the *i*-th reaction. For the typical conditions in a MWCVD diamond reactor using C_xH_y/H_2 mixtures, the major part (>90–95%) of the MW power absorbed by the electrons is converted by collisions into vibrational and rotational excitations of gas-phase molecules (H_2 and C_xH_y), and the remainder is used for dissociation of H_2 and C_xH_y molecules, plus molecular and atomic excitation and ionization. Subsequent collisions between the excited neutral molecules and ground-state molecules in the background gas distribute the excess energy around the plasma ball and cause it to heat up to a gas temperature of the order of 3000 K. At high temperatures ($T\geq 2800$ K), thermal dissociation of molecular hydrogen becomes a major source of the H atoms which initiate further production of the various hydrocarbon radical species necessary for diamond growth. Our calculations show that in order to predict correctly the gas temperature within a typical MW reactor using CH_4/H_2 gas mixtures and diamond growth conditions, it is necessary to take into account, as a minimum, three vibrational levels of H_2 (v=0,1,2), H_2 rotational and vibrational excitations (by electron impact) and de-excitation (vibrational-translational relaxation) by H atoms.

The gas-phase plasma chemistry and thermochemical input for H/C mixtures are taken from various sources including: the GRI-Mech 3.0 detailed reaction mechanism for neutral C_xH_y ($x\leq 2$, $y\leq 6$) species [33], [34] (plasma-chemical reactions), [35] (the electron-H_2 collision cross-sections), [36] (excitation of H_2 vibrational levels by electron impact), [37] (atomic hydrogen excitation cross-sections), [38] (C_xH_y ionization cross-sections). The plasma-chemical kinetics model includes ~210 direct and reverse reactions for 27 neutral species (C, CH, triplet-CH_2, singlet-CH_2, CH_3, CH_4, C_2(X), C_2(a), C_2H, C_2H_2, C_2H_3, C_2H_4, C_2H_5, C_2H_6, C_3, C_3H, C_3H_2, C_4, C_4H, C_4H_2, H, H_2 (v=0,1,2), electronic excited levels H(n=2), H(n=3), and H_2^*) and four charged species (electrons, ions $C_xH_y^+$, H_2^+, and H_3^+).

As in previous studies [7,39–41] the conservation equations for mass, momentum, energy, and species concentrations, together with appropriate initial and boundary conditions, thermal and caloric equations of state, are each integrated numerically until steady-state gas temperature and radicals distributions are attained. This process yields spatial distributions of the gas temperature, *T*, the flow field, and the various species number densities. The incorporation of gas-surface reactions (see ref. [12]), involving H abstraction to form surface monoradical and biradical sites, and the subsequent reactions of these sites with H and hydrocarbon radicals, serve to alter the gas composition close to the surface. The main effect of these reactions is to reduce the H atom concentrations directly above the growing diamond surface, which, in turn, affects the hydrocarbon radical concentration and has major implications for subsequent growth and its uniformity.

Previously, we assumed that we could use the value for $[H]_{ns}$ *near to* the surface calculated using the procedure above, as a good approximation to the value of $[H]_s$ *at* the surface. The subscript 'ns' means the concentration is specified at a grid node that is closest to the surface, at a distance of 0.5 d_z from the surface (d_z=1 mm is the grid cell size), while the subscript 's' means at the surface itself. However, for the high power density plasmas used for SCD growth our 2D model calculations showed that there can be a significant difference between the gas temperature near the substrate, T_{ns}, and the actual substrate temperature, T_s (*e.g.*, T_{ns}~1600 K but T_s=973 K). The chemical composition in such a thin thermal boundary layer

cannot be calculated accurately by a chemical mechanism with temperature-dependent reaction rates and with an assumed equilibrium thermal velocity and energy distribution based upon a given local temperature. Thus, this thin boundary layer is not included in our 2D and 3D models. But for growth mechanism and growth rate calculations, the true species fluxes arriving at the substrate are required. Therefore, we have estimated these fluxes as $N_{s,i}V_i/4$, where V_i is the thermal velocity of the i-th species and $N_{s,i}$ is the concentration of the i-th species at the surface. $N_{s,i}$ is determined from the concentrations calculated near the surface $N_{ns,i}$ as follows:

$$N_{s,i} = N_{ns,i}T_{ns}/T_s \qquad (10)$$

Here, we have assumed that the surface loss/production processes are not significant and species' mole fractions remain constant in the boundary layer. Since the concentration of some gas species can be a strong function of local gas temperature, this assumption will, for example, overestimate CH_x ($x<4$) concentrations at the surface in the case of a significant temperature drop $T_{ns}-T_s$ (which might occur in the high power MW discharge conditions, mentioned above). And, more importantly, this assumption is not true for atomic H under typical diamond CVD conditions because of substantial loss of H atoms at the substrate and substrate holder surfaces resulting from surface H abstraction and addition reactions. Therefore, we have taken these losses into account, in an approach similar to that used by Dandy and Coltrin [42].

$$DN\left([H]_{ns}/[N]_{ns} - [H]_s/[N]_s\right)/(0.5 \cdot d_z) = \gamma(T_s, H_s, H_2) \cdot V_H \cdot [H]_s/4 \qquad (11)$$

Here, N is the total gas concentration, and D is the diffusion coefficient for H in the reactive mixture. D (in units of $cm^2\ s^{-1}$) at a pressure p (in Torr) was approximated as $D=0.107\ T^{1.7}/p$ for diffusion of H in H_2. V_H is the hydrogen thermal velocity and the function $\gamma(T_s,H_s,H_2)$ is the atomic hydrogen loss probability, which can be expressed as

$$\gamma(T_s, H_s, H_2) = 0.83/\{1 + 0.3\ \exp(3430/T_s) + 0.1\ \exp(-4420/T_s)[H_2]_s/[H]_s\} \qquad (12)$$

taking into account the reactions of hydrogen abstraction (direct and reverse) and hydrogen addition [9,19].

One result of the heterogeneous loss of H atoms on the substrate and substrate holder surfaces is a sharp increase of H atom concentration near the substrate holder edge, which has been both observed experimentally [43] and simulated [16]. To avoid this non-uniformity preventing single crystal growth, the substrate holder size (of diameter D_{sh} in the case of a cylindrical substrate holder) should be larger than substrate diameter, D_s. For example, in order to simulate the SCD growth conditions of Bogdan *et al.* [28] (10% CH_4/90% H_2 mixture at 180 Torr, 600 W, T_s=973 K, the axial distance from the substrate to the top quartz window 42 mm), our calculations show that D_{sh} should be at least 8 mm to ensure a uniform growth rate across the 2.5×2.5 mm substrate. For smaller values of D_{sh} (*e.g.* D_{sh}= 6 mm), the calculation shows that radial profiles of the growth rate G and H atom concentration above the substrate have a minimum at r=0, and non-uniformity across the substrate of about 7%–10%. Such non-uniformity is in contradiction with the experimentally observed uniform growth rates. To study the effects of the substrate holder size and plasma volume V_p, all further 2D calculations of deposition processes were carried out for two different model cylindrical volumes, V_p, and two substrate holder diameters D_{sh}=9 mm and D_{sh}=12 mm, which provide almost uniform growth rate profiles.

Typical values of the plasma parameters obtained from the 2D model were as follows: maximum gas temperature T~3300 K and mean electron temperature T_e~1.3 eV for V_p~12 cm^3 (assuming the height H_p and diameter D_p of the cylindrical plasma region are about 1.8 cm and 2.9 cm, respectively, making the averaged absorbed power density Q_J~50 W cm^{-3}), and T~3300 K and T_e~1.5 eV for V_p~5 cm^3 (assuming H_p=1.6 cm and D_p=2 cm, so that Q_J~120 W cm^{-3}). The two power densities are significantly higher than those used for MCD growth (typically ~10–20 W cm^{-3}, assuming 1 kW MW power and D_p~H_p~5 cm, see *e.g.* ref. [44]), and as such, we shall refer to these two sets of conditions as the 'hot plasma' (Q_J~50 W cm^{-3}) and the 'extremely hot plasma' (Q_J~120 W cm^{-3}) conditions.

2D (r,z) distributions of gas temperature and mole fractions of selected species are shown in Figs. 4 and 5, for the extremely hot plasma conditions and D_{sh}=9 mm. Fig. 4(a) shows that the temperature distribution is fairly uniform across the centre of the plasma with a value remaining constant within the plasma ball of ~3300 K. The temperature drops significantly in the gap of a few mm between the plasma ball and the substrate surface, so that the gas temperature immediately above the growing diamond surface (T_{ns} in Eqs. (1) and (2)) is only around 1600 K. Fig. 4(b) shows the H atom

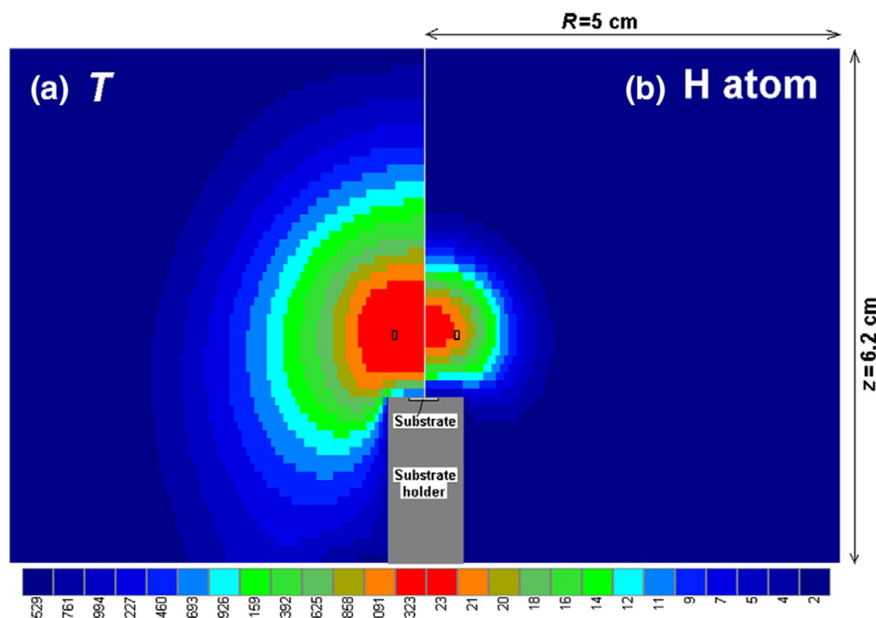

Fig. 4. 2D (r,z) plots of the calculated (a) gas temperature, T, in Kelvin and (b) H atom mole fraction expressed as a percentage, for substrate holder diameter D_{sh}=9 mm and power density ~120 W cm^{-3}. From the edge of the chamber to the centre the shading scale increases in 13 equal intervals from 297–529 to 3091–3323 K in (a), and from 0–2 to 21–23% in (b).

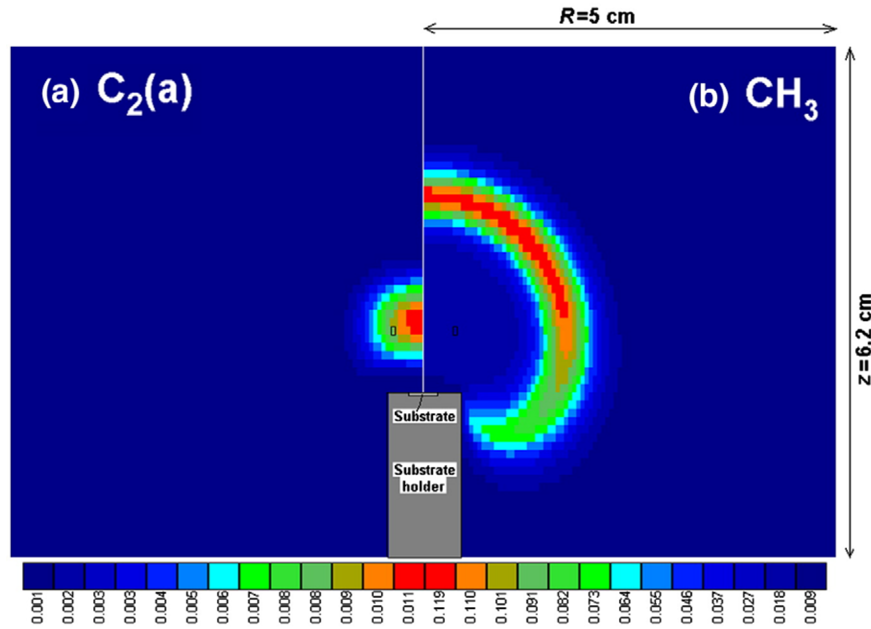

Fig. 5. 2D plots of the calculated (a) C_2(a) and (b) CH_3 mole fraction expressed as a percentage for substrate holder diameter D_{sh} = 9 mm and power density ~120 W cm^{-3}. From the edge of the chamber to the centre the shading scale increases in 13 equal intervals from 0–0.001 to 0.01–0.011% in (a), and from 0–0.009 to 0.11–0.119% in (b).

mole fraction expressed as a percentage, and as expected, the [H] is a maximum (23%) in the hottest region at the centre of the plasma ball but decays to ~1% at the substrate surface. Thus, there are a significant number of H atoms striking the surface that can initiate abstraction reactions and create the radical sites necessary for diamond growth.

Fig. 5 shows the mole fraction profiles for (a) C_2(a) and (b) CH_3. The C_2(a) concentration is very localised in the hot centre of the plasma ball where it is created, but outside of this region (including near the substrate surface) the concentration rapidly falls to negligible levels. It is worth noting that for CH_4/H_2 plasmas, emission from the Swan band of excited C_2 occurs over most of the visible region [45,46], and so produces most of the light that gives the plasma its apparent visual size, although there are lesser contributions from atomic H and from CH (but at 390 nm, which is just below the visible region for most people). Therefore, Fig. 5(a) predicts the visual appearance, size and shape of the plasma ball. Comparing this profile to the concentration profiles obtained for H (Fig. 4(b)) and CH_3 (Fig. 5(b)) we can see that that the visual extent of the plasma ball is not a reliable guide to the actual extent of the reactive plasma region. Fig. 5(b) emphasises this, since the [CH_3] maximises around the periphery of the hot gas region, and thus it is these regions that will be important for diamond growth. Therefore, it is important to realise that techniques which only measure species in the centre of the plasma ball region (*e.g.* laser spectroscopic methods) are, in effect, only obtaining circumstantial evidence toward the growth process.

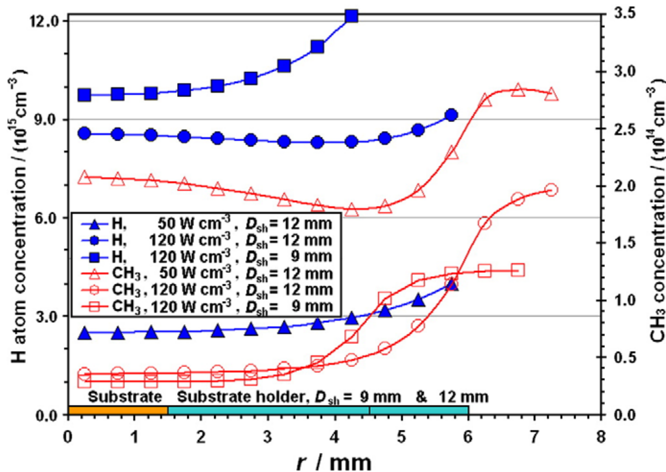

Fig. 6. Radial profiles of $[H]_s$ and CH_3 (r,z = 0.5 mm) concentrations above the surfaces of the substrate (D_s = 3 mm) and substrate holder (D_{sh} = 9 and 12 mm) for the two different absorbed power densities.

Radial distributions of atomic hydrogen concentration at the surface $[H]_s$ (calculated from the concentration of H 0.5 mm above the substrate and Eq. (11)) and CH_3 concentrations 0.5 mm above the substrate and substrate holder surface are shown in Fig. 6 for the hot plasma (D_{sh} = 12 mm) and extremely hot plasma (D_{sh} = 9 mm and D_{sh} = 12 mm) conditions. This figure illustrates the 'edge effects' of the substrate holder, and demonstrates why the D_{sh} needs to be much larger than D_s in order to achieve uniform concentration profiles above the surface, and hence uniform diamond growth. One can also see that the H atom concentration above the substrate increases by a factor of ~3.5 on increasing the plasma density from 50 to 150 W cm^{-3}, whereas the CH_3 concentration drops by ~6 times. Put another way, the ratio $[H]_s/[CH_3]_s$ increases from ~12 to ~240, roughly a factor of 20, as the plasma power density triples. Eq. (7) predicts that with this ratio increasing, the average crystal size should also increase. For these model conditions, Table 1 shows the calculated growth rates G and average crystal sizes $\langle d \rangle_{new}$. Predicted growth rates are uniform across the 2.5×2.5 mm substrate area, with values of G~2–2.5 µm h^{-1} for the extremely hot plasma conditions (120 W cm^{-3}) and G~8 µm h^{-1} for hot plasma conditions (50 W cm^{-3}). The observed experimental growth rates G~3–4 µm h^{-1} are between these calculated values. The dominant

Table 1
Growth rates, G, and average crystal sizes $\langle d \rangle$ (from Eq. (6)) and $\langle d \rangle_{new}$ (from Eq. (7)) calculated for the two different plasma conditions with substrate holder diameters (D_{sh}) of 9 and 12 mm

	'Hot plasma' 50 W cm^{-3}	'Extremely hot plasma' 120 W cm^{-3}	
	D_{sh} = 12 mm	D_{sh} = 12 mm	D_{sh} = 9 mm
$\langle d \rangle$/µm	0.27	5.1	7.1
$\langle d \rangle_{new}$/µm	3.2	1170	2250
G/(µm h^{-1})	8.3	2.34	2.0

Experimentally [28], the values were G~3–4 µm h^{-1} and $\langle d \rangle_{exp}$ >> 100 µm.

growth mechanism in these conditions is via CH_3 addition to monoradical sites (~75%), with CH_3 addition to biradical sites and CH_x addition to both sites having a lesser and roughly equal contribution.

The predictions of Eq. (7) for $\langle d\rangle_{new}$, show that the crystal size increases with power density and decreases with D_{sh}, which agrees with experimental observations that higher power, denser MW plasmas are needed for SCD growth. The value of $\langle d\rangle_{new}$ is ~3 μm for the hot plasma conditions and between 1170 and 2250 μm for the extremely hot plasma condition (depending upon which substrate holder diameter is used), which are consistent with the experimental report of near SCD growth over areas of 2.5×2.5 mm.

3. Conclusions

In this paper we have presented further evidence to support and refine our model [9,10,12] for the growth mechanisms of the various forms of diamond film, extending it to MW plasma systems and into the near SCD growth regime. A knowledge of the gas-phase concentrations near the growing diamond surface can be used to estimate the growth rate and average crystal size during diamond CVD, and thereby to predict whether the film morphology will be MCD, NCD, UNCD, and now SCD. The growth rate predictions give values that are very close to the experimental ones, showing that Eqs. (3) and (5) are reasonably reliable for the SCD growth regime. The amended version of the equation for $\langle d\rangle_{new}$, Eq. (7), gives crystal sizes which are consistent with those expected for SCD. However, the justification for including the correction factor (to change Eq. (6) into Eq. (7)) is not rigorous, and so Eq. (7) must be considered as somewhat empirical. Use of Eq. (7) to predict $\langle d\rangle_{new}$ values for (U)NCD and MCD growth conditions in HFCVD reactors indicates that the predictions for all these forms of diamond are also improved.

The qualitative trends predicted by Eq. (7) can provide useful indicators as to the experimental conditions that need to be achieved for SCD growth. First, a high plasma density is required to greatly increase the $[H]/[CH_3]$ ratio at the growing surface, which directly determines the average crystal size. But second, to have a reasonable growth rate, $[CH_3]$ must also be high. To achieve both these prerequisite conditions using standard laboratory MW sources (1–5 kW), the plasma ball needs to be only a couple of cm diameter, and this can often be attained by increasing the process pressures to over 100 Torr. But such small plasma balls mean that growing SCD films over areas larger than ~10 mm cannot be achieved using standard low power MW sources. For large area SCD growth, significantly more powerful (>30 kW) MW supplies will be needed to produce the necessary high plasma densities in large diameter plasmas, with all the technical and cost implications those incur. For the same gas mixtures and power densities, low substrate temperatures favour larger crystal sizes, however if T_s becomes too low growth rate drops significantly. A value of T_s~700°C seems the best compromise between growth rate and crystal size, however, efficient, uniform cooling to this value of large area substrates at the high plasma densities required is another important technical hurdle to be overcome. Finally, workers modelling the growth process or those characterizing their reactors should note that the reactive gas chemistry responsible for diamond growth extends well beyond the small, glowing region of the plasma visible to the eye. Thus, the visible extent of the plasma ball must not be taken as a reliable indicator of the true extent of the reactive region.

Acknowledgments

The authors would like to thank James Butler, Edward Crichton, Mike Ashfold and Andy Cheesman for useful discussions, and to Milos Nesládek for details of the MW reactor at IMO. YuAM wishes to thank RF for Key Science Schools grant No. 7101.2006.2 and ISTC for grant 2968/2005.

References

[1] P.W. May, Philos. Trans. R. Soc. Lond., A 358 (2000) 473.
[2] S.J. Harris, Appl. Phys. Lett. 56 (1990) 2298.
[3] D.G. Goodwin, J.E. Butler, in: M.A. Prelas, G. Popovici, L.K. Bigelow (Eds.), Handbook of Industrial Diamonds and Diamond Films, Marcel Dekker, New York, 1998.
[4] D.M. Gruen, O.A. Shenderova, A.Ya. Vul' (Eds.), Synthesis, Properties and Applications of Ultrananocrystalline Diamond, NATO Science Series part II, vol. 192, Springer, 2005.
[5] X. Xiao, J. Birrell, J.E. Gerbi, O. Auciello, J.A. Carlisle, J. Appl. Phys. 96 (2004) 2232.
[6] O.A. Williams, M. Daenen, J. D'Haen, K. Haenen, J. Maes, V.V. Moshchalkov, M. Nesládek, D.M. Gruen, Diamond Relat. Mater. 15 (2006) 654.
[7] P.W. May, J.A. Smith, Yu.A. Mankelevich, Diamond Relat. Mater. 15 (2006) 345.
[8] D. Zhou, T.G. McCauley, L.C. Qin, A.R. Krauss, D.M. Gruen, J. Appl. Phys. 83 (1998) 540.
[9] P.W. May, J.N. Harvey, J.A. Smith, Yu.A. Mankelevich, J. Appl. Phys. 99 (2006) 104907.
[10] P.W. May, Yu.A. Mankelevich, J. Appl. Phys. 100 (2006) 024301.
[11] J.R. Rabeau, P. John, J.I.B. Wilson, Y. Fan, J. Appl. Phys. 96 (2004) 6724.
[12] P.W. May, M.N.R. Ashfold, Yu.A. Mankelevich, J. Appl. Phys. 101 (2007) 053115.
[13] Y.F. Zhang, D. Dunn-Rankin, P. Taborek, J. Appl. Phys. 74 (1993) 6941.
[14] H. Yamada, A. Chayahara, Yoshiaki Mokuno, Y. Horino, N. Fujimori, Diamond Relat. Mater. 15 (2006) 522.
[15] B.W. Yu, S.L. Girshick, J. Appl. Phys. 75 (1994) 3914.
[16] Y.A. Mankelevich, A.T. Rakhimov, N.V. Suetin, Diamond Relat. Mater. 7 (1998) 1133.
[17] Y.A. Mankelevich, N.V. Suetin, M.N.R. Ashfold, W.E. Boxford, A.J. Orr-Ewing, J.A. Smith, J.B. Wills, Diamond Relat. Mater. 12 (2003) 383.
[18] S. Skokov, B. Weiner, M. Frenklach, J. Phys. Chem. 98 (1994) 7073.
[19] Y.A. Mankelevich, A.T. Rakhimov, N.V. Suetin, Diamond Relat. Mater. 5 (1996) 888.
[20] S.J. Harris, D.G. Goodwin, J. Phys. Chem. 97 (1993) 23.
[21] G.P. Smith, D.M. Golden, M. Frenklach, N.W. Moriarty, B. Eiteneer, M. Goldenberg, C.T. Bowman, R.K. Hanson, S. Song, W.C. Gardiner, Jr., V.V. Lissianski, Z. Qin, http://www.me.berkeley.edu/gri-mech/.
[22] E. Kondoh, T. Ohta, T. Mitomoto, K. Ohtsuka, Appl. Phys. Lett. 59 (1991) 488.
[23] J.R. Petherbridge, P.W. May, S.R.J. Pearce, K.N. Rosser, M.N.R. Ashfold, J. Appl. Phys. 89 (2001) 1484.
[24] D. Pradhan, Y.C. Lee, C.W. Pao, W.F. Pong, I.N. Lin, Diamond Relat. Mater. 15 (2006) 2001.
[25] T. Teraji, Phys. Status Solidi, A Appl. Res. 203 (2006) 3324.
[26] H. Yamada, A. Chayahara, Y. Mokuno, Y. Horino, S. Shikata, Diamond Relat. Mater. 15 (2006) 1738.
[27] G. Bogdan, M. Nesládek, J. D'Haen, J. Maes, V.V. Moshchalkov, K. Haenen, M. D'Olieslaeger, Phys. Status Solidi, A Appl. Res. 202 (2005) 2066.
[28] G. Bogdan, K. De Corte, W. Deferme, K. Haenen, M. Nesládek, Phys. Status Solidi, A Appl. Res. 203 (2006) 3063.
[29] J. Isberg, J. Hammersberg, E. Johansson, T. Wikström, D.J. Twitchen, A.J. Whitehead, S.E. Coe, G.A. Scarsbrook, Science 297 (2002) 1670.
[30] C.-s. Yan, H.-k. Mao, W. Li, J. Qian, Y. Zhao, R.J. Hemley, Phys. Status Solidi, A Appl. Res. 201 (2004) R25.
[31] S.S. Ho, C.S. Yan, Z. Liu, H.K. Mao, R.J. Hemley, Ind. Diamond Rev. (2006) 28 Jan.
[32] http://www.apollodiamond.com.
[33] G.P. Smith, D.M. Golden, M. Frenklach, N.W. Moriarty, B. Eiteneer, M. Goldenberg, C.T. Bowman, R.K. Hanson, S. Song, W.C. Gardiner, Jr., V.V. Lissianski, Z. Qin, http://www.me.berkeley.edu/gri-mech/.
[34] Yu.A. Mankelevich, A.J. Orr-Ewing, M.N.R. Ashfold, J. Appl. Phys. 102 (2007) 063310.
[35] A.G. Engelhardt, A.V. Phelps, Phys. Rev. 131 (1963) 2115.
[36] A. Klonover, U. Kaldor, J. Phys. B 12 (1979) 3797.
[37] P.M. Stone, Y.-Ki Kim, J. Res. NIST 107 (2002) 327.
[38] NIST Ref. data, http://physics.nist.gov/PhysRefData/Ionization/EII_table.html.
[39] Y.A. Mankelevich, N.V. Suetin, M.N.R. Ashfold, J.A. Smith, E. Cameron, Diamond Relat. Mater. 10 (2001) 364.
[40] M.N.R. Ashfold, P.W. May, J.R. Petherbridge, K.N. Rosser, J.A. Smith, Y.A. Mankelevich, N.V. Suetin, Phys. Chem. Chem. Phys. 3 (2001) 3471.
[41] J.A. Smith, J.B. Wills, H.S. Moores, A.J. Orr-Ewing, Yu.A. Mankelevich, N.V. Suetin, J. Appl. Phys. 92 (2002) 672.
[42] D.S. Dandy, M.E. Coltrin, J. Mater. Res. 10 (1995) 1993.
[43] S.A. Redman, PhD Thesis, School of Chemistry, Bristol University, UK, 1999.
[44] S.M. Leeds, P.W. May, E. Bartlett, M.N.R. Ashfold, K.N. Rosser, Diamond Relat. Mater. 8 (1999) 1377.
[45] T.S. McCauley, A. Israel, Y.K. Vohra, J.T. Tarvin, Rev. Sci. Instrum. 68 (1997) 1860.
[46] M.A. Elliott, P.W. May, J. Petherbridge, S.M. Leeds, M.N.R. Ashfold, Diamond Relat. Mater. 9 (2000) 311.